Design and Fabrication Issues on Micromachined Oxygen Sensors for Miniaturized Energy Consumption Measurement Systems

Chien-Chung Wu, Mei-Hsing Chen[1], Ching-Hsing Luo and Gwo-Bin Lee[1]*

Department of Electrical Engineering, National Cheng Kung University,
Tainan, Taiwan 701
[1]Department of Engineering Science, National Cheng Kung University,
Tainan, Taiwan 701

The size and cost of indirect calorimeters hinder their application in hospitals. This study employs micro-electromechanical systems MEMS techniques to develop oxygen sensors as one part of a miniaturized energy consumption measurement system for premature babies. Typically, the system is designed to operate at high oxygen concentrations. Accordingly, the current study deals with the development of oxygen sensors capable of sensing higher concentrations of oxygen at a low operation temperature of 150°C. The proposed gas sensors consist of a polysilicon resistor and a sensing metal-oxide film placed on a thermally isolated silicon-nitride membrane or bridge. The sensing film is a tin oxide sheet, which has been doped with a low concentration of 2wt% Li. This study involves the development of three different types of oxygen sensors, which are distinguished from each other by the structure of their microheaters. The first type is a microheater on a silicon nitride membrane, the second type employs a membrane located on a thin silicon layer, and the third type uses a bridge membrane with a thin underlying layer of silicon. At an operating temperature of 150°C, the power consumptions of these three sensors are found to be 24 mW, 223 mW and 1240 mW, respectively. The resulting experimental data indicate that the proposed oxygen sensors are capable of detecting oxygen with concentrations ranging from 21% to 50%, and that they exhibit a linear output behavior. These characteristics render the oxygen sensors suitable for use in most clinical applications within a hospital environment.

---

*Corresponding author, e-mail address: gwobin@mail.ncku.edu.tw

1.   Introduction

Clinical studies have revealed an increasing incidence of premature babies in recent years. It is essential that the health conditions of such infants be closely monitored, and this requires sophisticated clinical apparatus. A previous study reported that metabolic rate is a valuable indicator of the growth status of premature babies.[1] Currently, one of the most frequently adopted metabolic rate measurement methods is the so-called "Respiratory Quotient" (RQ) value, which is defined as the ratio of carbon-dioxide generation to oxygen consumption. Basically, the RQ value represents the oxidized substrates inside a body and, as such, provides clinical doctors with an important metabolic indicator. In general, the RQ value is equal to one for carbohydrates ($CO_2 : O_2 = 1$), 0.7 for fats, and 0.8 for proteins.[2] A reduction in the RQ value indicates a decreasing rate of carbohydrate metabolism and a shift towards alternative substrates such as proteins, and particularly fats. Previous studies have suggested that the quantity of proteins deposited is closely related to the protein intake and that the quantity of fat deposited is closely related to the energy intake.[3] Therefore, the RQ value provides a valuable indicator of a premature infant's energy intake.

Traditionally, RQ values have generally been determined by means of a noninvasive method, which employs a so-called "indirect calorimeter" in a flow-through technique.[4] In this technique, the respective concentrations of the oxygen and carbon-dioxide gases are measured during inspiration and expiration. However, any minor variations in the concentration of the oxygen tend to be diluted by the flow-through air, and thus it is generally necessary to employ high-precision gas analyzers when this technique is applied.[4] Furthermore, the indirect calorimeter is bulky and expensive with the result that it cannot be used routinely for clinical diagnosis and treatment. In order to overcome these limitations, we proposed a novel miniaturized energy consumption measurement system,[5] which employed a micro-gas sensing system comprising an oxygen sensor, a carbon-dioxide gas sensor, a humidity sensor, a temperature sensor, a flow-rate sensor and a system of micro-valves. Since the RQ measurement system requires the detection of oxygen consumption and carbon-dioxide gas generation, it will be placed on the infant's nose and must therefore be compact in size. Therefore, the present study proposes various types of micromachined oxygen sensors which can facilitate the development of miniaturized energy consumption measurement systems.

When designing the oxygen sensors, there are several issues to be taken into consideration, namely the detection range, the required sensitivity, selectivity and response time, the working temperature and the ability to scale down. Among these various considerations, the detection range and the working temperature are of particular importance for the applications addressed in the present study. For practical applications, the sensors should be able to detect oxygen concentrations in the range of 21% to 100%, and their operating temperature should be as low as possible in order to reduce their power consumption. A review of the available literature reveals that several different types of oxygen sensors have been reported, including, but not restricted to, the luminescence type,[6] the fiber-optic fluorosensor type,[7] the resistive type,[8-13] the galvanic cell type,[14] the clark cell-based type,[15] the limiting-current type,[16] the amperometric type,[17] the potentiometric type[18]

and the surface acoustic wave (SAW) type.[19] It has been reported that the silicon-based metal-oxide sensor offers several advantages over its counterparts.[8–13,20–22] In general, this sensor is compatible with IC processes, is compact in size and consumes low power. However, it suffers from lower selectivity and a slower response. Many researchers have investigated the potential applications of metal-oxide materials, whose resistivities depend strongly upon the ambient oxygen concentration. These materials include SnO_2, SnO_2+Li, TiO_2, Nb_2O_5, ZnO, Ga_2O_3, and $Gd_2Ti_2O_7$.[8–13] For example, Frank *et al.* considered the frequent application of a Ga_2O_3 thin film for detecting oxygen in furnaces or in automotive applications.[13] Furthermore, TiO_2-based sensors were shown to be suitable for detecting oxygen in the high-temperature and low-oxygen-concentration environment of an automobile exhaust.[8] However, several studies have noted that most of these materials usually require a rather high working temperature.[20,21] This condition is clearly unsuitable in clinical applications.

A further problem regarding metal-oxide films is their low sensitivity. The chemical sensing process comprises a variety of interaction steps, including physisorption, chemisorption, surface reaction, catalytic reaction, grain boundary reaction, bulk reaction and three-phase boundary reaction.[20] An oxygen molecule may capture an electron, turning into O^- or O_2^- or substituting an oxygen vacancy (Vo^{++}) on the surface of the metal-oxide film. Consequently, the chemisorption of an oxidizing gas such as oxygen may cause the conduction channel to disappear. Even though metal-oxide films exhibit a high sensitivity for reducing gases, they are rather insensitive for oxidizing gases. Previous researchers have indicated that the sensitivity of such films can be greatly improved by doping them with additives, which are then believed to act as catalysts to the redox reactions. For example, Sberveglieri *et al.* demonstrated the use of a Li-doped tin oxide film in improving the sensitivity of an oxygen sensor.[11]

As mentioned previously, the measurement of oxygen concentrations in excess of 21% is a vital requirement for miniaturized energy consumption measurement systems which are to be used in the monitoring of preterms. The present study involves the design of three types of microheater structures suitable for use in an oxygen sensor, and compares the power consumptions, reliabilities and yields for processing of each type. The first type is a microheater on a silicon nitride membrane, which can reduce the heating mass to minimize power consumption and improve the heating efficiency. The second type employs a membrane located on a thin silicon layer in order to promote the robustness of the microheater and simplifies the fabrication process. The third type uses a bridge membrane with a thin underlying layer of silicon, which enhances the robustness of the microheater and reduces the heating mass. Oxygen sensors which operate at a low temperature of approximately 150°C and are capable of detecting higher concentrations of oxygen are presented. The sensors comprise a polysilicon resistor and a sensing tin oxide film combined with the three different heater systems mentioned above. The polysilicon resistor serves as a heating element, which improves the sensitivity of the device. The sensitivity of the sensor is improved further by the use of a tin oxide sensing film doped with a low concentration of Li (2 wt%).

2.   Experimental Procedure

2.1 *Fabrication*

Figure 1 shows a schematic representation of the three different types of oxygen sensors. Every sensor consists of a polysilicon heater and a sensing film located on a thermally isolated silicon-nitride membrane, which is shown in Fig. 1(a). The polysilicon heater is used to heat the sensing film (tin oxide) and to enable the operation of the sensor at an appropriate temperature. In order to enhance the robustness of the device and simplify the fabrication process, a silicon-nitride membrane located on a thin silicon layer is constructed by controlled back-surface KOH silicon etching, as shown in Fig. 1(b). In order to enhance the robustness of the device and to minimize its power consumption, a suspended silicon-nitride bridge with a thin underlying layer of silicon is constructed by means of front-surface RIE etching and back-surface KOH etching. The entire sensing device is then located on this suspended structure, as shown in Fig. 1(c). The operation of the sensor relies upon the resistance of the tin oxide film varying appropriately when oxygen molecules are detected.

Figure 2 shows a schematic representation of the simplified fabrication process for three different types of oxygen sensors. Initially, an LPCVD process is used to deposit a thin layer (1 μm thick) of low-stress nitride on a double-sided polished p-type <100> Si substrate. This layer serves as a dielectric material and as a supporting membrane. The LPCVD process is then used to deposit and pattern a 0.5 μm polysilicon film as a heater, which has been implanted with boron ions in order to reduce its sheet resistance. Note that
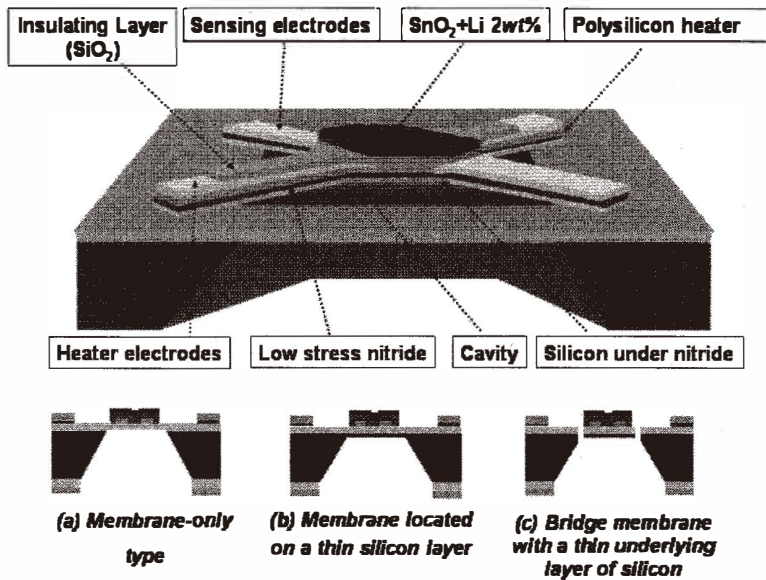
Fig. 1.   Schematic representation of three different types of oxygen sensors.
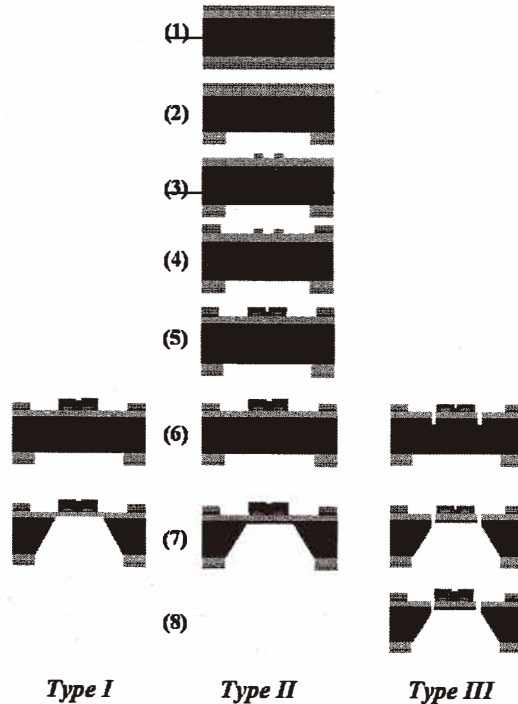
Fig. 2. Simplified fabrication process for three different types of oxygen sensors: TYPE I, (1) Low-stress nitride deposition and polysilicon deposition/doping/annealing, (2) Back-surface patterning, (3) Patterning of polysilicon heaters, (4) Deposition/patterning of Au electrodes, (5) Deposition/patterning of insulating layer (SiO$_2$), (6) Deposition of sensing layer (SnO$_2$+Li, 2 wt%) and (7) Complete back-surface silicon etching completely(KOH at 80°C); TYPE II (1)–(6) the same as TYPE I, (7) Incomplete back-surface silicon etching; TYPE III, (1)–(5) the same as TYPE I, (6) Patterning bridge structure (over etching by RIE), (7) Back-surface silicon etching and (8) Deposition of sensing layer.

after doping, the sheet resistance of the polysilicon film is 70 $\Omega/\square$. A Cr/Au (30 nm/500 nm thick) layer is then deposited using the E-Beam metallization process, followed by the sputtering of a SiO$_2$ (400 nm thick) film to serve as an electrical isolator between the heater and the sensing layer. A sensing material (SnO$_2$+Li, 2 wt%) film is deposited using the RF reactive sputtering system.[11,23] Finally, a back-surface KOH etching process of the Si is then performed using an one-sided etching apparatus. The difference between Type I and Type II is whether the silicon etching is complete or not.

The five preprocessing steps are the same in Type I and Type III. The bridge structure is then patterned by a front-surface RIE etching process. Note that an over-etching technique is performed in this step in order to form a bridge with a thin layer of silicon underneath. A back-surface KOH etching process of the Si is then performed using an one-sided etching apparatus. Finally, a sensing material film is deposited using the RF

sputtering system. Following completion of the fabrication process, the sensor chip is diced and packaged. A printed circuit board (PCB) with wire-bonded sensors is then designed for testing purposes. Figure 3 shows a photograph of a packaged chip with four oxygen sensors.

Figure 4 shows SEM images of the developed oxygen sensors. Figure 4(a) shows the membrane-only sensor type, Fig. 4(b) shows the sensor with a membrane and a thin
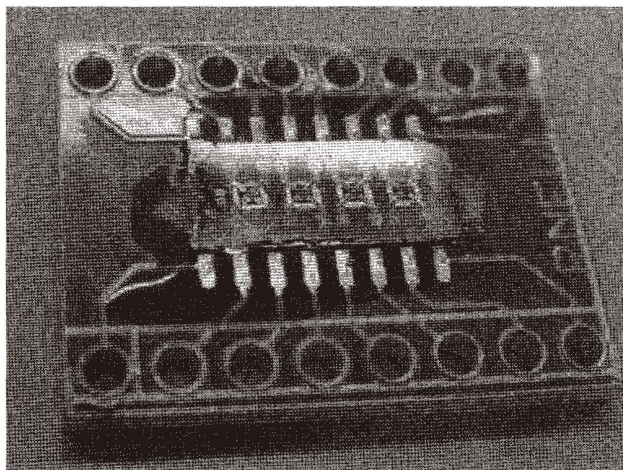
Fig. 3.   Photograph of chip with four oxygen sensors after packaging.
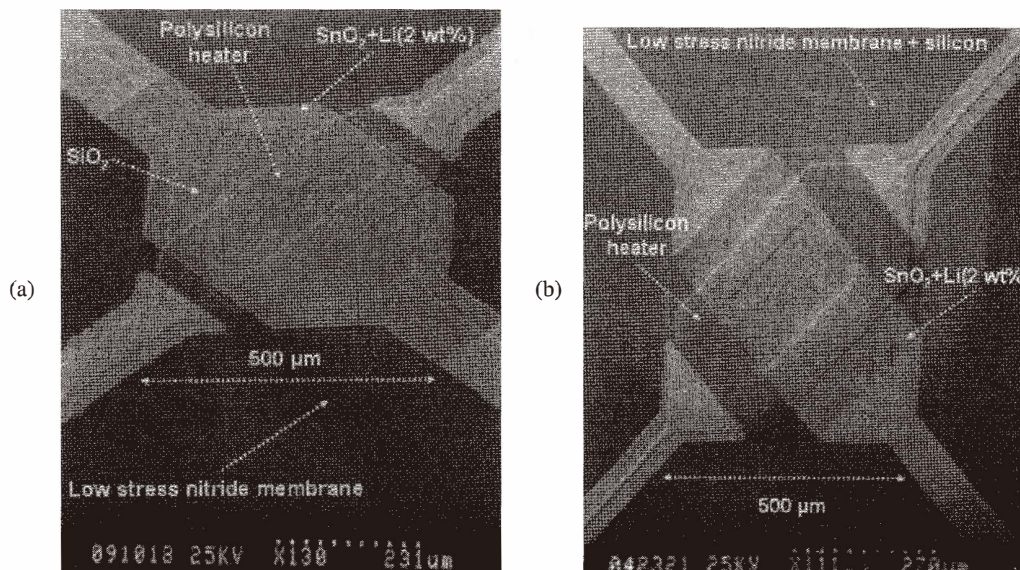
Fig. 4.   SEM images of different oxygen sensors.   (a) Membrane-only type and (b) Membrane located on a thin silicon layer.
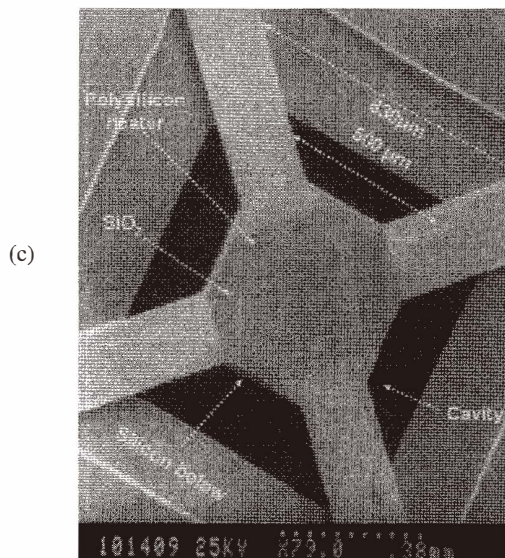
Fig. 4.   (continued from the previous page) (c) Bridge membrane with a thin underlying layer of silicon.

underlying layer of silicon, and Fig. 4(c) shows the sensor with a suspended bridge membrane and a thin underlying silicon layer. In all cases, the sensors have dimensions of 500 μm $\times$ 500 μm. Two sets of metal leads are used to provide driving voltages to the polysilicon resistors and to collect electrical signals induced by changes in the resistivity of the tin oxide films. As shown in the figure, the KOH anisotropic etching process used in the fabrication process generates a diaphragm silicon-nitride bridge with a thin underlying layer of silicon. The experimental data show that this design is successful in reducing the power consumption of the device.

2.2 *Experimental setup*

A programmable power supply (LPS 305/R/CE, MOTECH Industries Inc.) was used to provide electrical power to the polysilicon heater. The output signals from the sensing films were acquired through an ADC interface card (NI-6024E, National Instruments Inc.) using a Pentium II 300 MHz computer. Measurements for the sensors' resistances were conducted automatically using a LabVIEW program, and the oxygen concentration was varied automatically using Visual Basic programmable oxygen concentration software, which also controlled the flow rates of the oxygen through an RS-232C interface.

Figure 5 shows a schematic representation of the experimental setup employed for sensor calibration. It can be seen that three separate pipelines were used to supply pure oxygen (100%), room air (21% oxygen) and a vacuum for the calibration process. In practice, premature babies are provided with oxygen concentrations in excess of 21%. Although it is possible that a baby may be supplied with pure oxygen in extreme cases,
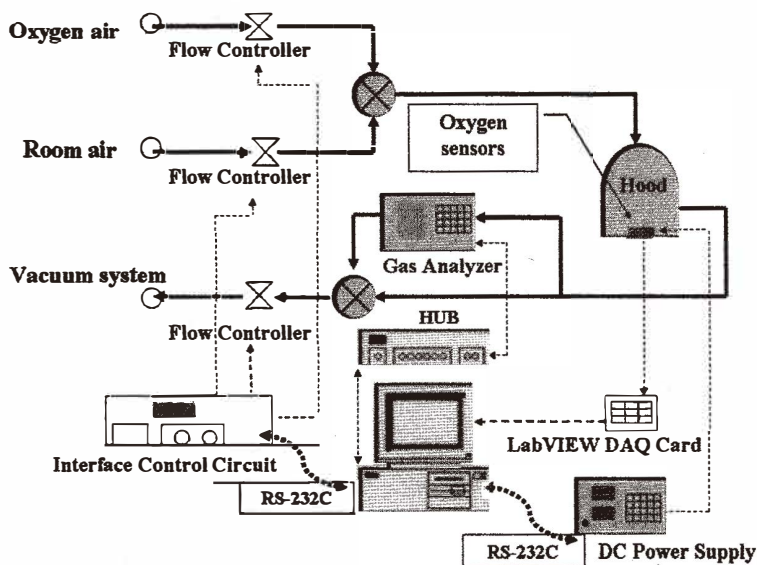
Fig. 5. Schematic representation of experimental setup for sensor calibration. (Note that a well-calibrated gas analyzer is used for calibration of the micromachined oxygen sensor.)

generally the oxygen concentration is maintained at a level below 40% in order to avoid retinal problems. Consequently, the oxygen concentrations during expiration are restricted to the range of 21% to 40%. Experimentally, oxygen concentrations ranging from 21% to 100% were prepared by mixing pure oxygen and room air. The precise concentration of oxygen was then measured using a well-calibrated differential paramagnetic oxygen analyzer (Magnos 16, Hartmann & Braun Inc.), which has the ability to measure the concentration of the oxygen with a resolution of 0.1%. Thermal images of the sensors were collected using an infrared micro-thermal imager with a resolution of 19 μm/pixel. (InfraScopeII™ system, Quantium Focus Instruments) to confirm their temperature distribution.

3.   Results and Discussion

Previous studies have shown that the operating temperature of the tin oxide film can affect the performance of the sensor significantly.[11] Many different types of microheaters have also been reported.[24,25] In the present study, a doped polysilicon resistor with a resistance of 1200 Ω was used to provide the necessary heating. Three different types of microheater structures were designed to facilitate oxygen concentration measurement. In order to minimize power consumption, the first type of microheater structure used a microheater placed on a low-stress nitride membrane with no underlying silicon layer, and was designed using a complete KOH anisotropic etching process. The second structure comprised a microheater placed on a low stress nitride membrane with a thin underlying

silicon layer. The strength of this device was improved using an incomplete KOH anisotropic etching process. The third type of structure incorporated a low-stress nitride bridge with a thin underlying layer of silicon, and was designed to improve both the robustness of the device and its power consumption characteristics.

Figure 6 shows the experimental relationship between the operating temperature and the power consumption for each of the three microheaters. It is clear that the operating temperature is linearly proportional to the power consumption for all three microheaters. At an operating temperature of 150°C, the results indicate that the power consumption for the microheater with only a membrane is 24 mW. For the heater comprising a bridge with a thin layer of silicon, it is 223 mW and in the case of a membrane with a thin underlying silicon layer it is 1240 mW.

Figure 7(a) shows the corresponding results for the membrane-only type of heater. The membrane fringes are approximately 55°C when the central region is 205°C, and the silicon substrate is roughly 40°C. Figure 7(b) shows the temperature distribution within the microheater comprised of a membrane with an underlying silicon layer. The results presented here suggest that this type of microheater consumes more power because heat is lost through the silicon layer. It is noted that the temperature at the fringes of the membrane is 88°C when the central region of the heater is at approximately 230°C, and when the silicon substrate temperature is 65°C. Finally, Fig. 7(c) shows that the membrane fringes
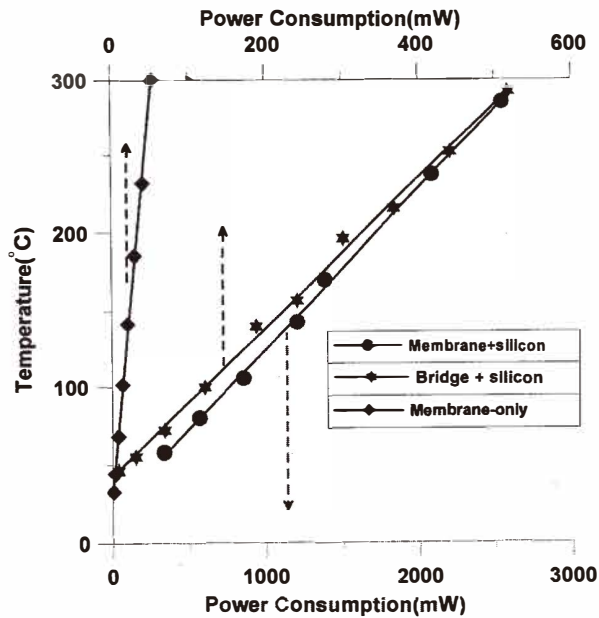
Fig. 6. Relationship between operating temperature and power consumption for different microheater types.
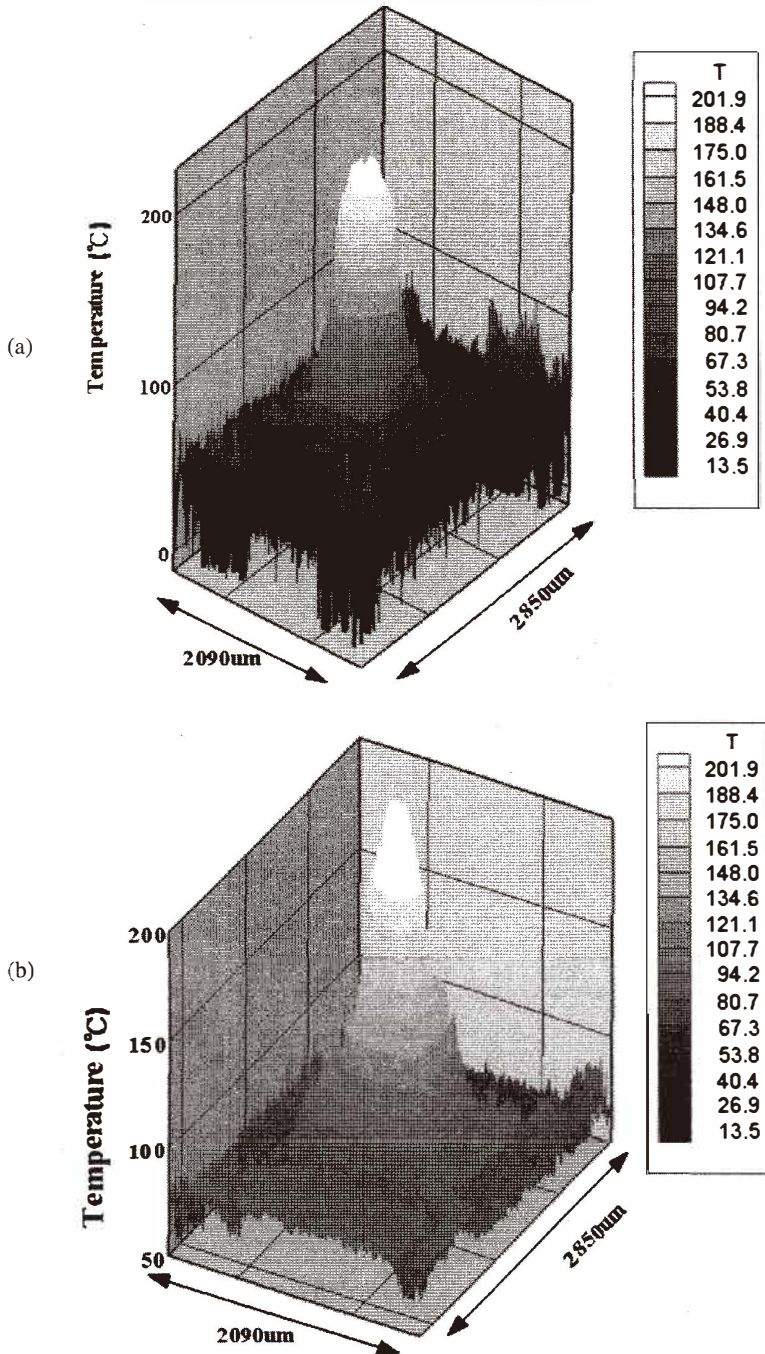
Fig. 7.   Thermal images of different microheater types. (a) Membrane-only type and (b) Membrane located on a thin silicon layer.
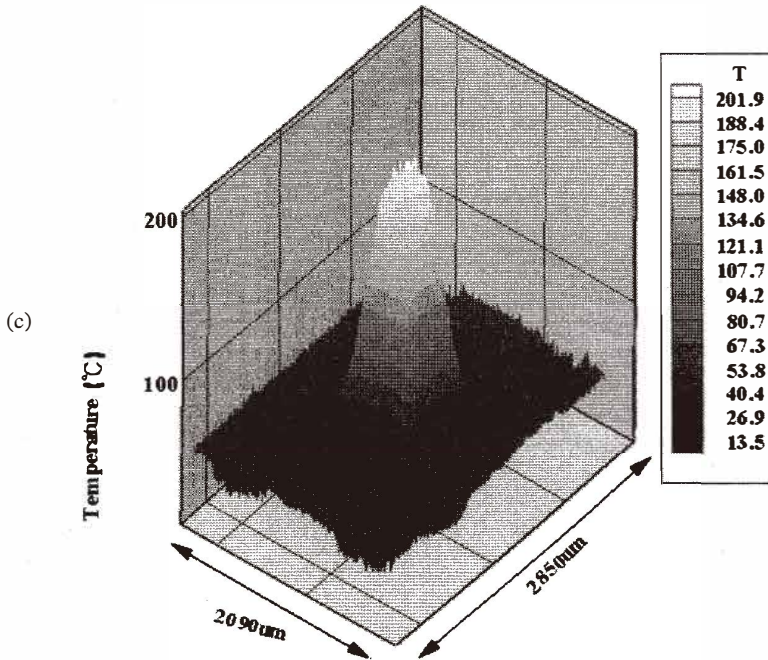
Fig. 7. (continued from the previous page) (c) Bridge membrane with a thin underlying layer of silicon.

are at a temperature of approximately 60°C when the center of the microheater is at approximately 200°C, and that the silicon substrate temperature is 50°C for the structure comprising a bridge with an underlying silicon layer.

The three microheaters were tested at a constant voltage mode at temperatures of 150°C and 300°C over extended periods of time. In the case of the membrane-only type, it was determined that when the device is maintained at a temperature of 300°C for one week, the membrane tends to buckle and breaks readily. Furthermore, when a square wave is used to trigger the heater electrodes, it was found that the membrane cycles through buckling and flattening stages, and that this again results in membrane breakage. However, the membrane proved to be more robust when subjected to step-wise wave heating rather than square wave heating. It was also noted that the membrane type is easily broken in post-processing assembly and packaging processes. Similar tests on the other two microheater structures revealed that they were more robust than the membrane-only type. (The corresponding experimental data are shown in Figs. 8(a)–(c)). Meanwhile, Fig. 8(d) presents the yields of the three devices in different testing modes and in processing. It can be seen that the yields of the microheater with a bridge and underlying thin silicon layer are lower because the device on the front side could easily be etched in the KOH etching process.

(a)

(b)

(c)

(d)
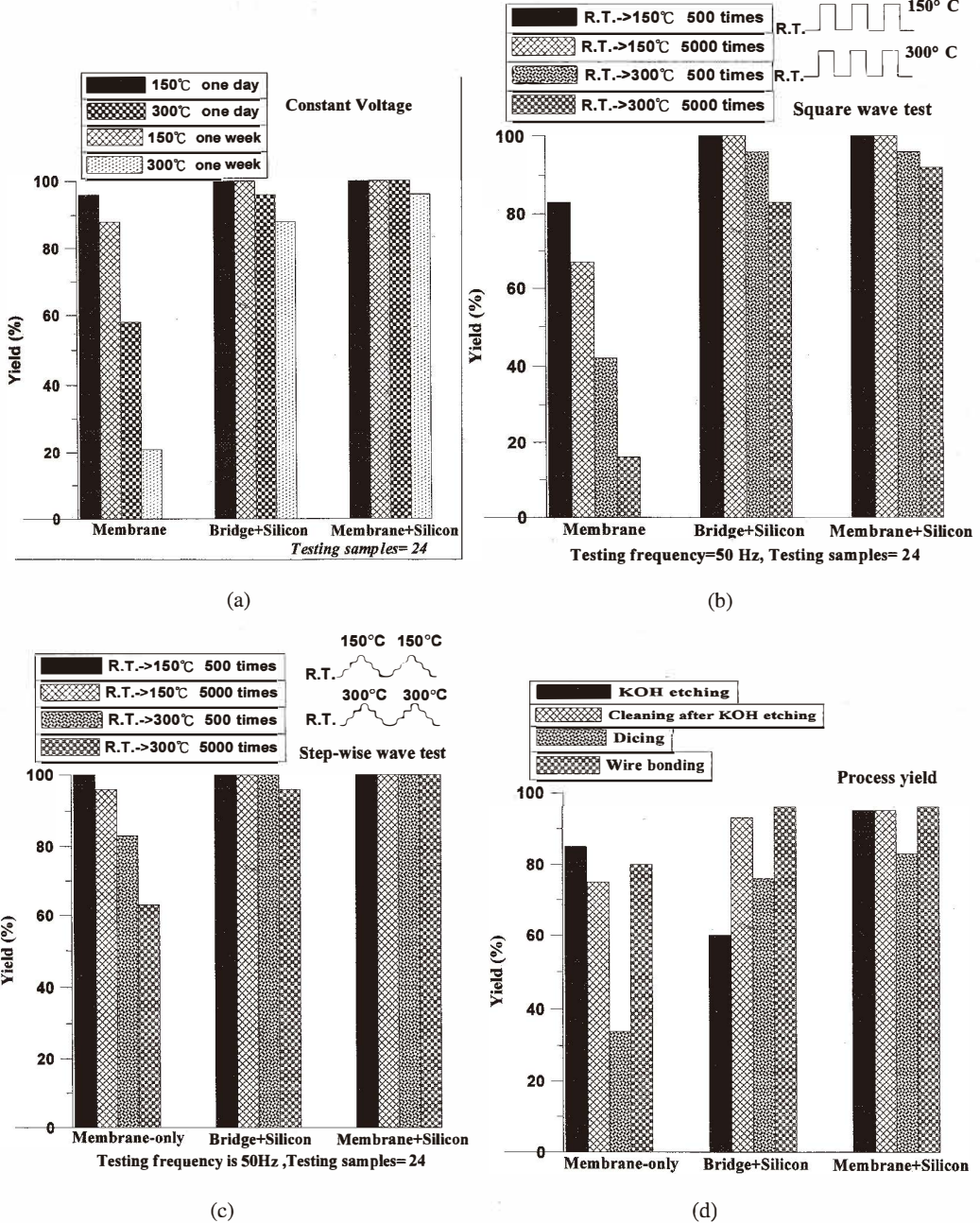
Fig. 8.   Yields of different microheater types in different testing modes and packaging. (a) The yields vs different kinds of microheater in constant voltage mode testing. (b) The yields vs different kinds of microheater in square wave mode testing. (c) The yields vs different kinds of microheater in step-wise wave mode testing. (d) The yield vs different kinds of microheater in processing.

In general, three types of processes occur when an oxygen molecule approaches the surface of the tin oxide-based gas sensor. The first process involves the physisorption of oxygen, in which an oxygen molecule is adsorbed onto the surfaces of oxygen vacancies or of other surface defects on the surface of the tin oxide. The oxygen molecules involved in this process are referred to henceforth as $O_{2(phys)}$. Note that electrons are not exchanged with the bulk atoms in this process. The second process is known as the ionosorption of oxygen, and describes the ionization of the adsorbed oxygen to become O_2^-, O^- or O^{2-}. This process occurs for the oxygen molecules which have been adsorbed onto the surface of the tin oxide and does involve the exchange of electrons with the bulk atoms. The third process is the desorption of oxygen, which involves electron transfer from the ionosorbed oxygen to the conduction band of the bulk.

It is known that tin oxide is conductive because of the existence of a high density of conduction electrons resulting from oxygen vacancies.[27] As described above, three different forms of oxygen ionosorption exist. These processes are strongly temperature dependent. At lower temperatures, i.e., from room temperature to approximately 150°C, the molecular form O_2^- dominates. The equation describing the oxygen physical adsorption can be expressed as follows.

$$O_{2(gas)} + S \rightleftharpoons O_{2(phys)} \tag{1}$$
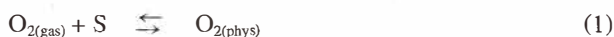
The equation describing the oxygen chemisorption can be expressed as follows.

$$O_{2(phys)} + e^- \rightleftharpoons O_2^- \tag{2}$$
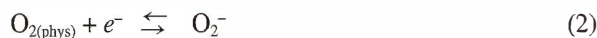
where S is an unoccupied chemisorption site, which represents a potential vacancy for the oxygen molecule on the tin oxide surface. Note that other surface defects also represent potential candidates for oxygen adsorption. When the temperature exceeds 150°C, measurements of the electron spin resonance on SnO_2 have shown that the ionosorbed oxygen is predominantly of the form O^-.[28] The oxygen chemisorption can be described as follows.

$$O_2^- + e^- \rightleftharpoons 2O^- \tag{3}$$

$$O_{2(phys)} + 2e^- \rightleftharpoons 2O^- \tag{4}$$

When the temperature exceeds 400°C, the adsorbed atoms are considered to be of the form O^{2-}.[29] In this temperature range, the equation describing the double-charged adsorbed oxygen is given by

$$O^- + e^- \rightleftharpoons O^{2-}. \tag{5}$$

However, O^{2-} is unstable if it does not react with the reducing gases such as CO and H_2 immediately or if it is trapped by an oxygen vacancy.[26] Thus in general O^{2-} is not expected to be present as an ionosorbed oxygen species. Previously, Lunsford has shown that the

reactivity of O^- is much higher than that of O_2^-.[30]

When the adsorption rate of oxygen is greater than the desorption rate, the conductance of the tin oxide film will decrease since the ionosorption process will capture more electrons from the bulk. Conversely, when the desorption rate exceeds the adsorption rate, the film conductance will increase as the desorption of oxygen releases free electrons to the conduction band.

Since the sensor performance is largely dependent upon its operating temperature, it is necessary to determine an optimum driving voltage. Accordingly, oxygen gases with constant concentrations in the range of 30–70% were supplied to the sensor comprising a bridge with an underlying silicon layer, and the sensing resistance was then measured as the driving voltage was varied between 10 and 24 v (0.5 v/step, 10-min wait/step). The corresponding experimental results are shown in Fig. 9. The results indicate that in the lower temperature range, the adsorption rate of oxygen increases linearly as the operating temperature rises. However, for higher operating temperatures, it is observed that the resistance of tin oxide decreases proportionally with increasing temperature. It is also
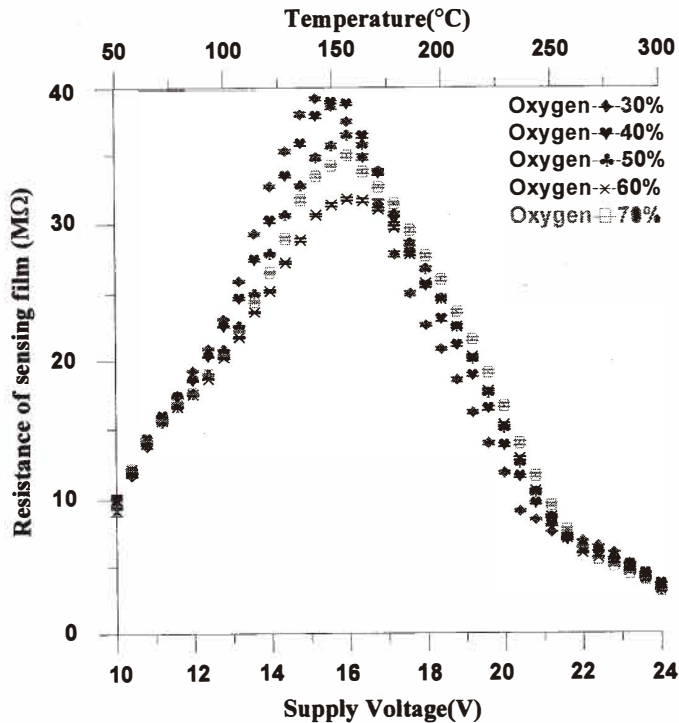
Fig. 9. Relationship between film resistance and supply voltage for oxygen concentrations in the range of 30% to 70%.

noted that the maximum device resistance occurs at virtually the same operating tempera-
ture irrespective of the oxygen concentration. It is noted that the sensor behavior in the
present study corresponds well with the results previously.[26] Based upon the results
presented in Fig. 9, an operating temperature of approximately 150°C was specified for the
sensor.

However, since chemisorption can only take place on the crystal defects of the film
surface, the ionic species only occupy about 2% of the total surface area at most.[27]
Furthermore, compared to the thermally excited chemisorption, the electron trapping-
releasing process is a slow dynamic process. Moreover, the application considered in the
present study concerns the measurement of high oxygen concentrations. These factors
imply that two issues must be considered; first, the adsorption of oxygen on the surface of
the tin oxide film will reach a saturation rate for higher oxygen concentrations, and second,
a long period of time must be allowed for the adsorbed oxygen to become fully desorbed
before testing the oxygen sensor with a different oxygen concentration. Figure 10 shows
the sensor response data for oxygen of different concentrations in the range of 30% to 70%.
Note that the measurement time is 10 min and that the sensor is then supplied with dry room
air with a relative humidity of 15% only for a 10-min stop period during which the
adsorbed oxygen is desorbed. Signals from a calibrated gas analyzer are shown in the same
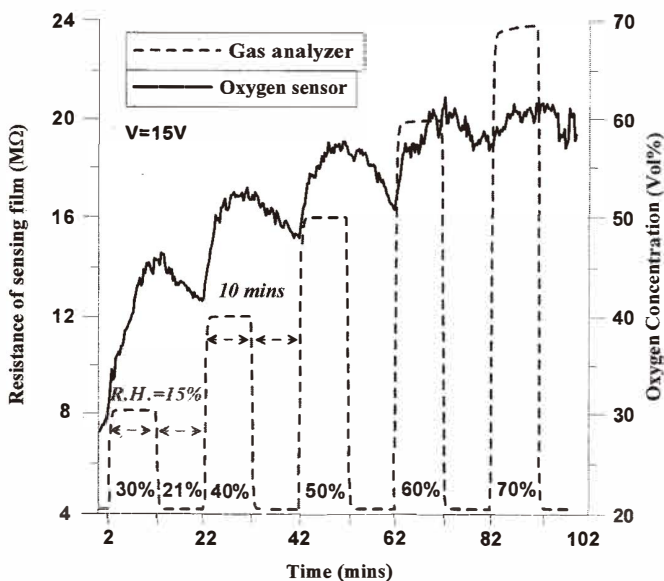
Fig. 10. Sensor response for oxygen concentrations in the range of 30% to 70%. (Note that the
measurement time is 10 min followed by a stop time of 10 min during which only dry room air with
a relative humidity of 15% is supplied to the sensor.)

figure for comparison. The results show that the sensing film resistance is not constant for a constant oxygen concentration, but tends to rise over time. Furthermore, it can be seen that as the oxygen concentration increases, the film resistance also increases, and the stop time of 10 min becomes insufficient to allow all of the adsorbed oxygen to fully desorb prior to the next testing cycle. Finally, it is noted that the insufficient desorption of oxygen molecules prior to the retesting of the sensor causes the resistance of the sensing film to reach a plateau value at oxygen concentrations in excess of 60%.

Water vapor is a further important consideration when using a tin oxide-based sensor. In the temperature range of 100°C to 500°C, interaction of the film with water vapor leads to the adsorption of water molecules (by physisorption or hydrogen bonding) and hydroxyl groups. In fact, IR studies show that at temperatures in excess of 200°C, water molecules are no longer present on the sensing film surface.[31]

It has been proven experimentally that the film surface conductivity increases when water vapor is present.[31] Two direct mechanisms have been proposed by Heiland and Kohl to explain this phenomenon.[32] A third, indirect, mechanism has also been presented by Morrison and by Henrich and Cox.[33, 34]

According to Heiland and Kohl, the role of an electron is as a donor to the 'rooted' OH group, which includes the lattice oxygen. They proposed the following equation:

$$H_2O_{(gas)} + Sn_{Sn} + O_o \; \underset{\rightarrow}{\leftarrow} \; (Sn_{Sn}^+ - OH^-) + (OH)_o^+ + e^-, \tag{6}$$

where $(Sn_{Sn}^+ - OH^-)$ represents an isolated hydroxyl or OH group and $(OH)_o^+$ denotes the rooted group. Having a lower electron affinity, the rooted OH group grows, and consequently can become ionized and become a donor.

The second mechanism takes into account the possibility of a reaction between the hydrogen atom and the lattice oxygen and the binding of the resulting hydroxyl group to the Sn atom. Through ionization, the resulting oxygen vacancy will produce additional electrons. The equation proposed by Heiland and Kohl[32] to explain this phenomenon is given by:

$$H_2O_{(gas)} + 2 \cdot Sn_{Sn} + O_O \; \underset{\rightarrow}{\leftarrow} \; 2 \cdot (Sn_{Sn}^+ - OH^-) + V_O^{++} + 2 \cdot e^-. \tag{7}$$
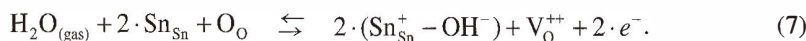
According to studies by Morrison and by Henrich and Cox, a third, indirect mechanism explains the increase in conductivity of the film surface in the presence of water vapor. They claimed that this effect could be the result of an interaction between either the hydroxyl group or the hydrogen atom originating from the water molecule with an acid or basic group, which are also acceptor surface states. Their electronic affinity could change after the interaction. Meanwhile, Henrich and Cox also proposed that the pre-adsorbed oxygen could be displaced by water adsorption.

Surface condition is a major factor in the three mechanisms presented above since surface steps and surface defects will tend to increase the dissociative adsorption. Furthermore, as shown by eq. (7), the presence of water vapor will increase the occurrence of oxygen vacancies. As oxygen vacancies are good candidates for oxygen adsorption, the

presence of water vapor will tend to increase oxygen adsorption on the film surface.

The oxygen sensors presented in this study are intended for use in a hospital environment, in which it can be expected that the relative humidity will be well controlled. In order to test the proposed sensors in a realistic environment, the relative humidity at National Cheng Kung Hospital in Tainan, Taiwan was first measured, and was found to be 60%. In the experiments described previously, dry room air with a relative humidity of 15% only was supplied to the sensor during the 10-min stop time. However, in a further experiment, a vacuuming process was used to purge the sensor hood with air with a relative humidity of 60%. Figure 11 shows the resulting sensor responses for oxygen of different concentrations over a 10-min measurement period followed by a 10-min recovery period. From the results, it is clear that the sensor performs well when measuring oxygen concentrations in the range of 21–50%. Furthermore, it is noted that a stop cycle of 10 min allows sufficient time for the receptivity of the sensing film to recover to its initial state. It confirms that the pre-adsorbed oxygen could be displaced by water adsorption, thus the performance of the sensor was improved. Accordingly, a response time of 10 min is specified for the proposed sensors in practical applications.

Figure 11 shows that the resistance of the sensing film increases over the measurement period. The change in resistance ($\Delta R \equiv R_{\text{final}} - R_{\text{initial}}$) during this period can be used to
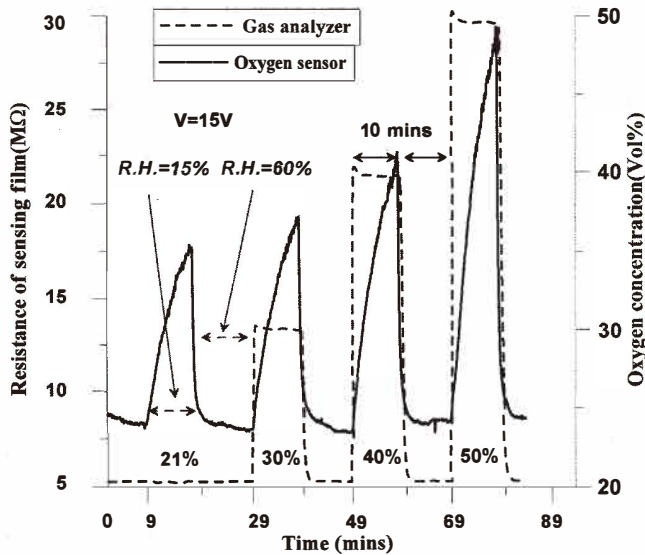
Fig. 11. Sensor response for oxygen concentrations in the range of 21% to 50%. (Note that the measurement time is 10 min followed by a stop time of 10 min during which air with a relative humidity of 60% is supplied to the sensor).
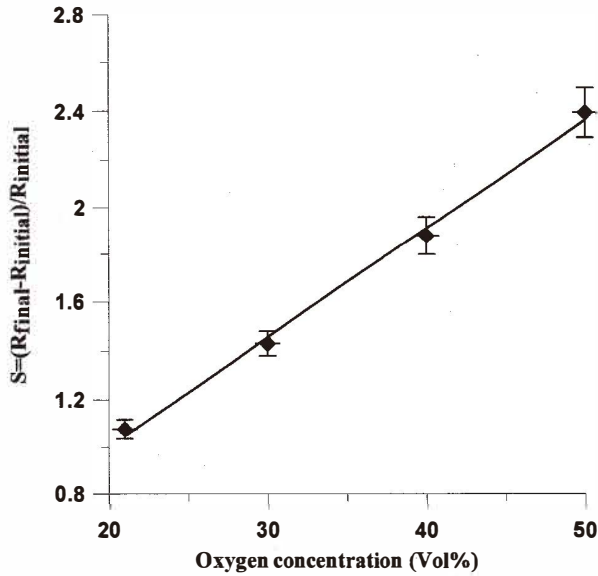
Fig. 12.   Relationship between sensor sensitivity and oxygen concentration.

characterize the relative sensitivity of the sensor, that is,

$$S \equiv \frac{R_{\text{final}} - R_{\text{initial}}}{R_{\text{initial}}}, \tag{8}$$

where R_{final} denotes the resistance value at the final measurement time and R_{initial} represents the initial resistance.

Figure 12 illustrates the relationship between the sensor relative sensitivity and the oxygen concentration, and shows that the sensor demonstrates a linear behavior over a range of oxygen concentrations from 21–50%.

4.   Conclusions

This study involved the development of compact oxygen sensors which are suitable for miniaturized energy consumption measurement systems used to monitor the growth status of premature babies. Three different types of microheaters have been fabricated using micromachining techniques, and have been compared under the same experimental conditions. It has been shown that the membrane-only type has a lower power consumption than the microheaters suspending on a silicon nitride membrane with a thin underlying silicon layer. For the microheaters which employ a thin silicon layer, the results have shown that the bridge type is more power efficient. Furthermore, it has been demonstrated that the

membrane with a thin underlying silicon layer provides the most robust microheater structure, while the membrane-only type is the most prone to breakage.

This study makes two major contributions. It has shown that the proposed sensors are capable of detecting oxygen with low operating temperatures, and that the power consumption for the microheater with a membrane only is 24 mW. For the heater comprising a bridge with a thin layer of silicon, it is 223 mW. In the case of a membrane with a thin underlying silicon layer, it is 1240 mW at an operating temperature of 150°C. Second, the proposed oxygen sensors provide linear output signals in the detection of oxygen with concentrations ranging from 21% to 50%.

Acknowledgements

References

1   T. F. Yeh, L. D. Lilien, S. T. Leu and R. S. Pildes: Biol. Neonate **46** (1984) 157.

2   A. C. Guyton and J. E. Hall: Text Book of Medical Physiology 9E (W. B. Saunders Company Publishing, Philadelphia, 2000) Chap. 71.

3   G. Zoppi, A. Luciano, M. Cinquetti, S. Graziani and M. Bolognani: Eur. J. Clin. Nutr. **52** (1998) 360.

4   J. L. Change, C. H. Luo and T. F. Yeh: Rev. Sci. Instrum. **67** (1996) 535.

5   C. C. Wu, G. B. Lee, C. H. Luo and W. S. Hwang: The Seventh World Congress on Biosensors 2002(Biosensors, Kyoto, Japan, 2002) p. P3–6.03.

6   Y. G. Ma, T. C. Cheung, C. M. Che and J. C. Shen: Thin Solid Films **333** (1998) 224.

7   O. S. Wolfbeis, L. J. Weis, M. J. P. Leiner and W. E. Ziegler: Anal. Chem. **60** (1988) 2028.

8   R. K. Sharma, M. C. Bhatnagar and G. L. Sharma: Sensor Actuat. B **46** (1998) 194.

9   I. Kosacki and H. L. Tuller: Sensor Actuat. B **24** (1995) 370.

10   M. Egashira, N. Kanehara, Y. Shimuzu and H. Iwanaga: Sensor Actuat. B **18** (1989) 349.

11   G. Sberveglieri, G. Faglia, S. Groppelli, P. Nelli and C. Perego: Sensor Actuat. B **13** (1993) 117.

12   J. Atkinson, A. Cganny and C. S. de Cloke: Sensor Actuat. B **47** (1998) 171.

13   J. Frank, M. Fleischer, H. Meixner and A. Feltz: Sensor Actuat. B **49** (1998) 110.

14   H. Ogino and K. Asakura: Talanta **42** (1995) 305.

15   S. J. Liu, H. X. Shen and J. X. Feng: Anal. Chimica Acta. **313** (1995) 89.

16   K. Ishibashi, T. Kashima and A. Asada: Sensor Actuat. B **13** (1993) 41.

17   Y. Miyahara, K. Tsukada, Y. Watanable and Y. Shibata: Sensor Actuat. B **20** (1994) 89.

18   T. Eguchi and J. Kuwano: Mater. Res. Bull. **30** (1995) 1351.

19   D. M. Oglesby, B. T. Upchurch, B. D. Leighty, J. P. Collman, X. Zhang and P. C. Herrmann: Anal. Chem. **66** (1994) 2745.

20   W. GÖpel and D. Schierbaum: Sensor Actuat. B **26** (1995) 1.

21   H. Meixner and U. Lampe: Sensor Actuat. B **33** (1996) 198.

22   L. Y. Sheng, Z. Tang, J. Wu, C. H. Chan and K. O. Sin: Sensor Actuat. B **49** (1998) 81.

23   V. V. Kissine, S. A. Voroshilov and V. V. Sysoev: Sensor Actuat. B **55** (1999) 55.

24   K. H. Fung, Z. Tang, C. H. Chan, K. O. Sin and W. Cheung: Sensor Actuat. A **54** (1996) 482.

25   I. Simon, N. Bârsan, M. Bauer and U. Weimar: Sensor Actuat. B **73** (2001) 1.

26   J. Ding, T. J. McAvoy, R. E. Cavicchi and S. Semancik: Sensor Actuat. B **77** (2001) 597.

27   J. Watson, K. Ihokura and G. S. V. Coles: Meas. Sci. Technol. **4** (1993) 711.

28   S. C. Change: J. Vaccum Sci. Technol. **17** (1980) 366.

29   Y. Mizokawa and S. Nakamura: Oyobutsuri **46**(1997) 580.

30   J. H. Lunsford: Catalyst Rev. **144** (1973) 751.

31   N. Barsan and U. Weimar: J. Electroceram. **7** (2001) 143.

32   G. Heiland and D. Kohl: in Chemical Sensor Technology, Vol. 1, ed. T. Seiyama (Kodansha, Tokyo, 1989) p. 15.

33   S. R. Morrison: The Chemical Physics of Surfaces 2nd edn. (Plenum Press, New York, 1990) Chap. 4.

34   V. A. Henrich and P.A. Cox: The Surface Science of Metal Oxides (University Press, Cambridge, 1994) Chap. 3.